Gravity Wave Emission in an Atmosphere-like Configuration of the Differentially Heated Rotating Annulus Experiment

Journal:	*Journal of Fluid Mechanics*
Manuscript ID:	JFM-13-S-0886.R2
mss type:	Standard
Date Submitted by the Author:	n/a
Complete List of Authors:	Borchert, Sebastian; Goethe-Universitaet Frankfurt, Institut fuer Atmosphaere und Umwelt Achatz, Ulrich; Goethe-Universitaet Frankfurt, Institut fuer Atmosphaere und Umwelt Fruman, Mark; Goethe-Universitaet Frankfurt, Institut fuer Atmosphaere und Umwelt
Keyword:	Baroclinic flows < Geophysical and Geological Flows, Internal waves < Geophysical and Geological Flows, Rotating flows < Geophysical and Geological Flows

Gravity Wave Emission in an Atmosphere-like Configuration of the Differentially Heated Rotating Annulus Experiment

Sebastian Borchert[1]†**, Ulrich Achatz**[1]
and Mark D. Fruman[1]

[1]Institut für Atmosphäre und Umwelt, Goethe-Universität Frankfurt, Altenhöferallee 1,
D-60438, Frankfurt am Main, Germany

A finite-volume model of the classic differentially heated rotating annulus experiment is used to study the spontaneous emission of gravity waves (GWs) from jet stream imbalances, which may be an important source of these waves in the atmosphere and for which no satisfactory parameterisation exists. Experiments were performed using a classic laboratory configuration as well as using a much wider and shallower annulus with a much larger temperature difference between the inner and outer cylinder walls. The latter configuration is more atmosphere-like, in particular since the Brunt-Väisälä frequency is larger than the inertial frequency, resulting in more realistic GW dispersion properties. In both experiments, the model is initialised with a baroclinically unstable axisymmetric state established using a two-dimensional version of the code, and a low-azimuthal mode baroclinic wave featuring a meandering jet is allowed to develop. Possible regions of GW activity are identified by the horizontal velocity divergence and a modal decomposition of the small-scale structures of the flow. Results indicate GW activity in both annulus configurations close to the inner cylinder wall and within the baroclinic wave. The former is attributable to boundary layer instabilities, while the latter possibly originates in part from spontaneous GW emission from the baroclinic wave.

Key words: Authors should not enter keywords on the manuscript, as these must be chosen by the author during the online submission process and will then be added during the typesetting process (see http://journals.cambridge.org/data/relatedlink/jfm-keywords.pdf for the full list)

1. Introduction

Internal gravity waves (GWs) play an important role in both oceanic and atmospheric dynamics (Müller *et al.* 1986; Fritts & Alexander 2003; Kim *et al.* 2003; Alexander *et al.* 2010). Radiated from various processes in the atmosphere, they are typically too small in scale to be explicitly resolved by present-day numerical weather prediction or climate models. They have, however, a significant effect on the resolved flow and therefore pose an important multi-scale problem. GWs in the atmosphere are typically divided into orographic, generated by flow over topography, and non-orographic, mostly due to convective processes, and spontaneous imbalance. The relative importance of these

† Email address for correspondence: borchert@iau.uni-frankfurt.de

2   *S. Borchert, U. Achatz and M. D. Fruman*

waves and their sources is seasonally dependent (Sato *et al.* 2009). While flow-dependent parameterisations for orographic and convectively forced GWs do exist (Palmer *et al.* 1986; McFarlane 1987; Chun & Baik 1998; Beres *et al.* 2004; Chun *et al.* 2004; Beres *et al.* 2005; Song & Chun 2008; Richter *et al.* 2010), less progress has been made in the cases of the other sources, of which spontaneous imbalance of synoptic-scale flow might be the most important. Observations identifying increased GW activity in the vicinity of jet stream exit regions (Uccellini & Koch 1987; Guest *et al.* 2000; Pavelin *et al.* 2001; Plougonven *et al.* 2003) are evidence that large-scale (balanced) flows can and do spontaneously radiate GWs. Directly applying the concept of geostrophic adjustment (Rossby 1938; Uccellini & Koch 1987; Fritts & Luo 1992; Luo & Fritts 1993; O'Sullivan & Dunkerton 1995; Pavelin *et al.* 2001) to the parameterisation of GW emission is difficult since the system is continuously re-establishing an unbalanced flow that sheds imbalances by GW radiation. Ford (1994*a*,*b*,*c*) applied the concept of Lighthill radiation (Lighthill 1952) to GWs radiated from vortices in shallow-water flow, but certain assumptions for this theory are violated for GW radiation from jet streams. Recent work by Snyder *et al.* (2009) and Wang & Zhang (2010) indicates that the process can be understood to a large extent by linear models, in which the GWs are solutions of a system linearised about a balanced state and forced by the residual tendency. It was found that the accuracy of these models depends on the choice of balance used to define the background flow. When quasi-geostrophic dynamics is used, systematic deviations from the fully nonlinear dynamics develop after a while (Snyder *et al.* 2009). This could be improved on by obtaining the background flow from a higher-order balance (Wang & Zhang 2010).

Obviously, examining these processes in the atmosphere confronts the scientist with particular challenges. Due to its extreme complexity, GW emission will always be embedded in the interaction of a multitude of interdependent processes, many of which are not detectable from analysis or campaign data. The benefits of repeated and more detailed measurements, while representing the only source of information about the real atmosphere, are limited by the non-repeatability of an atmospheric situation. The same event never occurs twice. This argues for complementary laboratory experiments, which provide a more focused dialogue between experiment and theory. An especially interesting scenario in the context of spontaneous imbalance is GW emission from jet streams in baroclinic-wave life cycles (O'Sullivan & Dunkerton 1995; Zhang 2004; Viúdez & Dritschel 2006; Plougonven & Snyder 2007), which are also examined in laboratory experiments using the differentially heated rotating annulus (Hide 1958). In that experiment, a fluid is confined between two cylindrical walls, with the outer wall kept at a higher temperature than the inner, and the entire apparatus is mounted on a rotating table. At sufficiently fast rotation this set-up leads to a baroclinic instability closely related to that which is believed to be the core process of mid-latitude cyclogenesis. A survey of the flow regimes observed in the experiment is found in Hide & Mason (1975). Promising laboratory experiments on wave generation observed at the interface between two superposed fluids of differing density have been done by Lovegrove *et al.* (1999, 2000) and Williams *et al.* (2003, 2005, 2008) for a baroclinically unstable flow in the rotating annulus, and by Afanasyev (2003) for colliding vortex dipoles in a non-rotating experimental set-up. A variant of the conventional differentially heated rotating annulus, where in addition to the horizontal temperature gradient, an external vertical temperature gradient is applied, is discussed by Miller & Fowlis (1986) and Hathaway & Fowlis (1986) and modelled by Kwak & Hyun (1992). In this version of the experiment, the stratification of the fluid can be controlled independently of the lateral temperature gradient. Here, however, we stick with the conventional set-up, as it seems to be a configuration more favoured in the experimental physics community. GWs have been identified in a version of a classic annu-

lus set-up with continuous stratification (Jacoby *et al.* 2011; Randriamampianina 2013), but they have been shown to be probably due to boundary-layer instabilities instead of spontaneous emission by baroclinic waves. By a classic set-up we mean an annulus with an outer cylinder radius of about 10 cm, a gap width between inner and outer cylinders of less than 10 cm and a fluid depth of about 10 cm. The lateral temperature difference in a typical classic configuration is about 10 K and the angular velocity ranges from 0 to about 5 rad/s (0 to about 48 revolutions per minute) (Hide & Mason 1975).

Using a newly developed finite-volume algorithm for Boussinesq flow in a rotating annulus (Borchert *et al.* 2014) we focus on two experiments, the first using a classic laboratory configuration of the annulus, the parameters of which are very close to those used in a laboratory experiment by Harlander *et al.* (2011), and the second using a much wider and shallower configuration with a much larger temperature difference between the inner and outer walls. In the latter, side walls naturally have much less influence on the interior flow, and the ratio of the Brunt-Väisälä frequency N to the inertial frequency f – essential parameters in the GW dispersion and polarisation relations – is greater than unity, as is the case in the real atmosphere. The present work is limited to the identification of GW activity in the two annulus configurations. The investigation into the mechanism of spontaneous GW emission in the annulus and what portion of the GW field originates from this source will be presented elsewhere. Section 2 describes the physical parameters and the numerical model used in the study. This is followed in section 3 by an analysis of the factors that simultaneously control N/f and baroclinic instability in the rotating annulus, leading to the identification of a more atmosphere-like annulus configuration. Section 4 describes our findings with regard to the GW activity in both the classic and atmosphere-like configurations. Finally section 5 summarises the results and gives a short discussion.

2. The model

A detailed description of the model and its numerical implementation in the *cylindrical flow solver with implicit turbulence model* (cylFloit) is given by Borchert *et al.* (2014). We summarise here only those features necessary for understanding the present text.

2.1. *Geometry*

A schematic view of the differentially heated rotating annulus is given in figure 1. It consists of two coaxial cylinders mounted on a rotating table. The inner cylinder, of radius a, is cooled to the constant temperature T_a and the outer cylinder, of radius b, is heated to the temperature T_b such that, usually, $T_a < T_b$. The gap between the cylinders is filled with water up to an equilibrium depth d. The surface in the laboratory experiment considered here is free, and hence depends on horizontal location and time. In the numerical model, however, we approximate it by an inviscid rigid lid. The apparatus rotates at the angular velocity Ω. The cylindrical coordinates are the azimuth angle ϑ, the radial distance from the axis of rotation r, and the vertical distance from the bottom z.

2.2. *Governing equations*

Since deviations $\Delta\hat{\rho}$ from the constant background density of the fluid $\hat{\rho}_0$ at reference temperature $T_0 = (T_a + T_b)/2$ are generally relatively small ($|\Delta\hat{\rho}| \ll \hat{\rho}_0$), the fluid-dynamical equations are used in the Boussinesq approximation. We took these equations from Farnell & Plumb (1975, 1976) and Hignett *et al.* (1985) and used them in flux form, adapted

4   *S. Borchert, U. Achatz and M. D. Fruman*

to a finite-volume discretisation. The pressure $\hat{p}$ is split into a time-independent reference pressure $\hat{p}_0$ and the deviation $\Delta\hat{p}$ therefrom. The reference pressure is defined by the hydrostatic equilibrium between the pressure gradient force, gravity, and the centrifugal force, i.e.

$$\boldsymbol{\nabla}\hat{p}_0 = \boldsymbol{g}\hat{\rho}_0 - \left[\boldsymbol{\Omega} \times (\boldsymbol{\Omega} \times \boldsymbol{r})\right]\hat{\rho}_0, \tag{2.1}$$

where $\boldsymbol{\nabla} = \boldsymbol{e_\vartheta}(1/r)\partial/\partial\vartheta + \boldsymbol{e_r}\partial/\partial r + \boldsymbol{e_z}\partial/\partial z$, $\boldsymbol{g} = -g\boldsymbol{e_z}$ is the gravitational force, $\boldsymbol{\Omega} = \Omega\boldsymbol{e_z}$ is the angular-velocity vector, and $-\boldsymbol{\Omega} \times (\boldsymbol{\Omega} \times \boldsymbol{r}) = \Omega^2 r\boldsymbol{e_r}$ is the centrifugal force. Here $\boldsymbol{e_\vartheta}$, $\boldsymbol{e_r}$ and $\boldsymbol{e_z}$ are the azimuthal, radial and vertical unit vectors. The dynamics are then described relative to the reference state by subtracting (2.1) from the full momentum equation and applying the Boussinesq approximation to get

$$\frac{\partial\boldsymbol{v}}{\partial t} = -\boldsymbol{\nabla} \cdot (\boldsymbol{vv} + p\boldsymbol{I} - \sigma) - 2\boldsymbol{\Omega} \times \boldsymbol{v} + \boldsymbol{g}\rho - \left[\boldsymbol{\Omega} \times (\boldsymbol{\Omega} \times \boldsymbol{r})\right]\rho, \tag{2.2}$$

where $p \coloneqq \Delta\hat{p}/\hat{\rho}_0$, $\rho \coloneqq \Delta\hat{\rho}/\hat{\rho}_0$ and $\boldsymbol{v} = u\boldsymbol{e_\vartheta} + v\boldsymbol{e_r} + w\boldsymbol{e_z}$ is the velocity vector. The first term on the right-hand side is the divergence of the symmetric total momentum flux tensor, which consists of the advective flux of mass-specific momentum, described by the dyadic product $\boldsymbol{vv}$, the density-specific pressure tensor, with the unit tensor $\boldsymbol{I}$, and the viscous stress tensor

$$\sigma = \nu\left[\boldsymbol{\nabla}\boldsymbol{v} + (\boldsymbol{\nabla}\boldsymbol{v})^{\mathrm{T}}\right], \tag{2.3}$$

where ν is the kinematic viscosity and $\boldsymbol{\nabla}\boldsymbol{v}$ is the velocity-gradient tensor. The superscript T denotes the transpose. The flux term in (2.2) is followed by the Coriolis force and the reduced gravitational and centrifugal forces. The governing equations are completed by the continuity equation

$$\boldsymbol{\nabla} \cdot \boldsymbol{v} = 0, \tag{2.4}$$

the thermodynamic internal energy equation

$$\frac{\partial T}{\partial t} = -\boldsymbol{\nabla} \cdot (\boldsymbol{v}T) + \boldsymbol{\nabla} \cdot (\kappa\boldsymbol{\nabla}T), \tag{2.5}$$

and the equation of state

$$\rho = \rho_1(T - T_0) + \rho_2(T - T_0)^2, \tag{2.6}$$

where T is temperature, κ is the thermal diffusivity, $T_0 = (T_a + T_b)/2$ is the constant reference temperature, and $\rho_{1,2}$ are coefficients depending on the working fluid. The viscosity ν and thermal diffusivity κ vary with temperature according to

$$\nu = \nu_0\left[1 + \nu_1(T - T_0) + \nu_2(T - T_0)^2\right], \tag{2.7}$$

$$\kappa = \kappa_0\left[1 + \kappa_1(T - T_0) + \kappa_2(T - T_0)^2\right], \tag{2.8}$$

where $\nu_{0,1,2}$ and $\kappa_{0,1,2}$ are six more fluid-dependent coefficients. Eqs. (2.6), (2.7) and (2.8) are parameterisations for the dependence of ρ, ν and κ on the temperature. The coefficients $\rho_{1,2}$, $\nu_{0,1,2}$ and $\kappa_{0,1,2}$ were derived by fitting parabolas to tabulated values for water between $10\,^\circ\mathrm{C}$ and $70\,^\circ\mathrm{C}$ (at pressure of $1000\,\mathrm{hPa}$) taken from Verein Deutscher Ingenieure *et al.* (2006), Section Dba 2, and are listed in table 1 (note that they depend on T_0). The coefficient of correlation (see, e.g., Clapham & Nicholson 2009) between fit and data was greater than 0.99 for all fits.

2.3. *Boundary conditions*

Periodic boundary conditions are used in the azimuthal direction. The velocity satisfies no-slip and no-normal flow conditions (i.e. the velocity is identically zero) at the radial

boundaries and at the bottom. The experimental set-up described by von Larcher & Egbers (2005) and Harlander *et al.* (2011) has a free fluid surface. We assume that the free surface displacements are small compared to the equilibrium depth at rest d in the annulus set-ups considered here. Thus a stress-free rigid lid may be a good approximation for the free surface, i.e. the vertical velocity component vanishes as do the vertical derivatives of both horizontal velocity components (James *et al.* 1981). Another common experimental set-up where a lid is brought into contact with the fluid surface (Hide & Mason 1975), which would be modelled by the no-slip boundary condition, is not considered here. Temperature is prescribed at the radial boundaries, with $T(r = a) = T_a$ and $T(r = b) = T_b$. At the model bottom and model top vanishing heat flux is assumed, i.e. the vertical temperature derivative vanishes there.

2.4. *Discretisation*

A finite-volume method is used to solve the flow equations numerically. The code has been adapted from an algorithm for the solution of the pseudo-incompressible equations in the atmosphere (Rieper *et al.* 2013), by modifying it to solve the Boussinesq equations, introducing a regular cylindrical-coordinate finite-volume grid, and by modifying the boundary conditions. The annulus volume is subdivided into volume cells of azimuthal angular width $\Delta\vartheta$, radial width Δr and vertical extension Δz. A staggered C-grid (Arakawa & Lamb 1977) is used so that the cell for each velocity component is centred on the temperature-cell face to which it is normal. The algorithm is constructed so as to implement an implicit parameterisation of subgrid-scale (SGS) through a special handling of the advective fluxes. Instead of constructing the fluxes from the surrounding volume averaged velocities by high-order interpolation, a weighted average of first-, second- and third-order accurate interpolations is used. The weights used in this *adaptive local deconvolution method* (ALDM) (Hickel *et al.* 2006) have been chosen so that the numerical viscosity and diffusivity of the odd-order interpolation optimally mimic the effect of the unresolved eddies. In a variety of complex turbulent flows including decaying turbulence (Hickel *et al.* 2006), boundary layer flows (Hickel & Adams 2007, 2008), separated flows (Hickel *et al.* 2008) and stratified turbulence (Remmler & Hickel 2012), ALDM has proven to perform as well as established explicit SGS models like the dynamic Smogorinsky model (Germano *et al.* 1991). A low-storage third-order Runge-Kutta method (Williamson 1980) is used for the discretisation in time, with an adaptive timestep determined from the instantaneous velocity field. The Poisson equation for the dynamic pressure is solved iteratively using a preconditioned biconjugate gradient stabilised (BiCGSTAB) method (e.g. Meister 2011).

3. An atmosphere-like annulus configuration

3.1. *Results from a classic configuration*

In all simulations to be discussed here we have first obtained an azimuthally symmetric asymptotic steady state by integrating the model in a two-dimensional (2D, without azimuthal dependence) mode over a sufficiently long time span t_{2D} from a resting initial state with homogeneous pressure $p = 0$ and temperature $T = T_0 = (T_a + T_b)/2$. The full model was then initialised with the obtained 2D steady state and a random low-amplitude temperature perturbation. For a large enough temperature difference between the inner and outer cylinders, baroclinic instability sets in and a baroclinic wave develops, transporting heat in the direction opposite to the large-scale radial temperature gradient. The first experiments presented here are from a classic laboratory configuration, the parameters of which are given in table 1. Its main characteristics are inner and outer

6   *S. Borchert, U. Achatz and M. D. Fruman*

cylinder radii of $a = 4.5$ cm and $b = 12$ cm, fluid depth $d = 13.5$ cm, lateral temperature difference of $T_b - T_a = 8$ K, and rotation rate $\Omega = 0.63$ rad/s (6 rpm). These values are from an experiment presented in Borchert *et al.* (2014) and are very close to parameters used in a laboratory experiment by Harlander *et al.* (2011). Parameters for the numerical model are given in table 2. The column "coarse 1" in table 2 lists the spatial resolution as well as t_{2D}, and the amplitude of the random temperature perturbations used to initialise the corresponding 3D simulation. Figure 2 shows snapshots of the horizontal temperature and horizontal-velocity distribution. Vertical cross sections of the azimuthally symmetric steady state temperature field as well as the azimuthally averaged temperature in the presence of the baroclinic waves are depicted in figure 3.

In order to get an idea of the radial and vertical structure of the stratification of the annulus flow, we introduced the local ratio N_l/f, where the local azimuthal-mean squared Brunt-Väisälä frequency is

$$N_l^2 = -g\overline{\frac{\partial \rho}{\partial z}}^{\vartheta},   \tag{3.1}$$

where $\overline{(\cdot)}^{\vartheta}$ denotes averaging over the azimuthal coordinate, and $\rho = \Delta\hat{\rho}/\hat{\rho}_0$. The distribution of N_l/f is shown in figure 3c. Stratification in the experiment is brought about by an overturning cell consisting of upwelling of warm liquid near the outer cylinder and downwelling of cool liquid near the inner cylinder. The ratio N_l/f resulting from this is very different from that occurring in the real atmosphere. In the upper troposphere of mid-latitudes, the ratio is on the order of 100 (e.g. Esler & Polvani 2004), while in the classical annulus configuration, it is on the order of 0.1. This affects GWs both quantitatively and qualitatively. The intrinsic frequency of plane GWs $\hat{\omega}$ satisfies, in the Boussinesq approximation, the dispersion relation (e.g. Gill 1982; Fritts & Alexander 2003)

$$\hat{\omega}^2 = \frac{N^2\left(k^2 + l^2\right) + f^2 m^2}{k^2 + l^2 + m^2} = N^2 \cos^2(\alpha) + f^2 \sin^2(\alpha),   \tag{3.2}$$

where k and l are the two horizontal wave number components, m is the vertical wave number, and $\alpha = \arctan(m/\sqrt{k^2 + l^2})$ is the angle of phase propagation relative to the horizontal plane. While in the atmosphere high-frequency waves exhibit near-horizontal phase propagation, and low-frequency waves propagate more vertically, conditions in the classic differentially heated rotating annulus lead to the opposite behaviour. In the rest of this section we will describe a configuration of the annulus that, at least qualitatively, better represents real-atmosphere conditions.

3.2. *Theoretical considerations*

Using the equation of state (2.6) our estimate for N/f is

$$\frac{N}{f} = \frac{\sqrt{g\left|\rho_1\left(T_b - T_a\right)\right|\chi_z/d}}{f},   \tag{3.3}$$

where N is the global and time average Brunt-Väisälä frequency

$$N = \left(\frac{1}{\mathcal{T}}\int_{\mathcal{T}} dt\, \overline{N_l^2}^{r,z}\right)^{1/2},   \tag{3.4}$$

and

$$\chi_z = \frac{d}{\rho(T_b) - \rho(T_a)}\frac{1}{\mathcal{T}}\int_{\mathcal{T}} dt\, \frac{1}{V}\int_V dV\, \frac{\partial \rho}{\partial z}   \tag{3.5}$$

is the vertical density gradient, averaged over the total annulus volume V not occupied by the boundary layers (the approximate thicknesses of which are given further below) and over a sufficiently long period of time $\mathcal{T}$ and normalized by the density gradient expected to leading order from the overturning circulation (Hide 1967). In (3.4), $\overline{(\cdot)}^{r,z}$ denotes averaging over the radial and vertical coordinates excluding the boundary layers. The expectation $\chi_z \sim 1$ is actually rather an upper limit since the baroclinic waves reduce the radial temperature difference available for inducing a stratification via the overturning circulation. Based on (3.3), there are several options available for increasing N/f. We do not pursue switching to a fluid with a higher thermal expansion coefficient ρ_1, leaving us with increasing the temperature difference $T_b - T_a$ and decreasing the fluid depth d and the angular velocity Ω.

Care must be taken not to suppress baroclinic instability. Quasi-geostrophic theory (Charney 1948) can be used as a guideline (e.g. Vallis 2006). For convenience we neglect friction and heat conduction in the following considerations. Furthermore, at a representative mid-radius position $\Omega^2(a+b)/2 \ll g$ for the annulus configurations considered here so the centrifugal force may also be neglected (Hide 1958; Williams 1967). The Boussinesq equations can then be written

$$\frac{D\boldsymbol{u}}{Dt} = -f\boldsymbol{e_z} \times \boldsymbol{u} - \boldsymbol{\nabla_h} p, \tag{3.6a}$$

$$\frac{Dw}{Dt} = B - \frac{\partial p}{\partial z}, \tag{3.6b}$$

$$\frac{DB}{Dt} = 0, \tag{3.6c}$$

$$\boldsymbol{\nabla_h} \cdot \boldsymbol{u} + \frac{\partial w}{\partial z} = 0, \tag{3.6d}$$

where $D/Dt = \partial/\partial t + \boldsymbol{v} \cdot \boldsymbol{\nabla}$ is the material derivative, $\boldsymbol{u}$ is the horizontal velocity, w is the vertical velocity, $\boldsymbol{\nabla_h}$ is the horizontal part of the nabla operator, and $B = -g\rho$ is the buoyancy. The anelastic equations are used by Vallis (2006), e.g., as the starting point for the derivation of quasi-geostrophic theory. These only differ from the Boussinesq equations here by an altitude-dependent reference density. Characteristic horizontal velocity and length scales U and L, together with the inertial frequency, are used to define the Rossby number

$$Ro = \frac{U}{fL}. \tag{3.7}$$

In the limit $Ro \ll 1$, the thermal wind relation can be used to obtain an estimate for the (azimuthal) velocity scale U. Choosing in addition $L = b - a$ for (3.7) yields the *thermal* Rossby number (Hide 1967)

$$Ro_{th} = \left(\frac{N}{f}\frac{d}{b-a}\right)^2 \frac{\chi_r}{\chi_z} = Bu\frac{\chi_r}{\chi_z}, \tag{3.8}$$

where Bu is the Burger number (e.g. Read *et al.* 1997; Bastin & Read 1998) and

$$\chi_r = \frac{b-a}{\rho(T_b) - \rho(T_a)} \frac{1}{\mathcal{T}} \int_{\mathcal{T}} dt \frac{1}{V} \int_V dV \frac{\partial \rho}{\partial r} \tag{3.9}$$

is the normalised mean radial density gradient (Hide 1967). Ro_{th} can be used as a rough estimate for the true Rossby number. Assuming for convenience $\chi_r \sim 1$ and thus $\chi_r/\chi_z \sim 1$, Ro_{th} is determined by the squared product of N/f and the annulus aspect ratio

8   *S. Borchert, U. Achatz and M. D. Fruman*

$d/(b-a)$. Strongly stratified flow configurations with $N/f > 1$ must be shallow for quasi-geostrophic theory to hold to leading order, i.e. $d/(b-a) < 1$ is required.

Following Eady (1949), one can assume a background flow with $N^2 =$ const. and an azimuthal velocity, given by the thermal wind relation, of the form $\bar{u} = \Lambda z$ (where Λ is a constant), in order to keep the problem tractable. Although the Eady model is formulated for a zonally periodic rectangular channel on the f plane, it can yield a rough understanding of the observed behaviour if the dominant unstable scales in the annulus are considerably less than the radial distance from the center of rotation, so that curvature terms can be neglected (e.g. Allen 1972; Hide & Mason 1975). We thus make use of the following results from the Eady model (see, e.g., Vallis 2006). It is found that modes of the quasi-geostrophic approximation to (3.6) linearised about the background flow can only grow if the approximated instability criterion

$$Bu = \left(\frac{N}{f}\frac{d}{b-a}\right)^2 < \left(\frac{\mu_c}{\pi}\right)^2 \tag{3.10}$$

is satisfied, where $\mu_c = 2.399$ and $(\mu_c/\pi)^2 = 0.583$ (e.g. Hide & Mason 1975; Vallis 2006). Thus, the aspect ratio $d/(b-a)$ must be kept sufficiently small while decreasing d and f and increasing $T_b - T_a$ in order to maximise the ratio N/f. Therefore, a slowly rotating wide and shallow annulus with a relatively large temperature difference between the inner and outer walls is needed.

Another consideration concerns the boundary layers. Let

$$\delta_E = d\,Ek^{\frac{1}{2}}, \tag{3.11}$$

$$\delta_S = (b-a)\,Ek^{\frac{1}{3}}, \tag{3.12}$$

$$\delta_T = d\left(\frac{\kappa_0\nu_0}{g\,|\rho_1\,(T_b - T_a)|\,d^3}\right)^{\frac{1}{4}} \tag{3.13}$$

be, respectively, the approximate thicknesses of the viscous Ekman layer at the bottom, the viscous Stewartson layer at the side walls, and the thermal boundary layer at the side walls, where

$$Ek = \frac{\nu_0}{\Omega d^2} \tag{3.14}$$

is the Ekman number (Farnell & Plumb 1975; James *et al.* 1981). Strictly speaking (3.11) and (3.12) are only valid for homogeneous fluids. For stratified fluids the boundary layer thicknesses at bottom and side walls have modified forms (Barcilon & Pedlosky 1967a,b). Nevertheless, we assume the simpler formulas (3.11) and (3.12) are sufficient for our purposes. Applying the above modifications of the annulus parameters, the Ekman number will increase and so will the fraction of the fluid depth taken up by the Ekman layer and of the gap width taken up by the Stewartson layer. At some point viscosity might substantially affect the dynamics in the interior, which would be undesirable if one is interested in the dynamics of the free fluid flow.

Furthermore the ratio of the area of the free fluid surface S_{top} to the area of the total annulus surface $S_{\partial V}$ (free fluid surface, cylinder walls and bottom)

$$\frac{S_{top}}{S_{\partial V}} = \frac{1}{2\left(1 + \frac{d}{b-a}\right)} \tag{3.15}$$

will also increase with decreasing aspect ratio so that the neglect of all thermal exchange processes between fluid and air becomes more and more questionable when relatively

high temperatures are imposed on the outer cylinder wall in order to increase the radial temperature gradient. In a laboratory version of the experiment it might be necessary to place a lid slightly above the fluid surface to minimise thermal fluxes and air drag (Williams 1969). In general, we endeavour to keep the model parameters of our numerical simulations within the limits of experimental practicability.

3.3. *Large-scale dynamics simulated in a newly suggested configuration*

In table 1 we list the parameters of a suggested atmosphere-like annulus configuration, which were finally chosen as a compromise between our goal to increase N/f and the restrictions mentioned above. It has inner and outer cylinder radii of $a = 20\,\text{cm}$ and $b = 70\,\text{cm}$ and a fluid depth of $d = 4\,\text{cm}$. The lateral temperature difference is $T_b - T_a = 30\,\text{K}$ and it rotates with $\Omega = 0.08\,\text{rad/s}$ (0.76 rpm). The spatial dimensions of the new configuration are close to values proposed by Rossby (1926) for an experiment imitating the atmospheric flow and to the dimensions of the early rotating dishpan experiments by Riehl & Fultz (1957).

The spatial resolution and run time of a 2D simulation using the atmosphere-like annulus configuration, as well as the amplitude of the random temperature perturbation in a corresponding 3D simulation, are listed in table 2 (in the column "coarse 1"). Figure 4 shows snapshots of the temperature and horizontal-velocity distribution at mid-depth from the 3D simulation, and figure 5 shows vertical cross sections of the azimuthally averaged temperature field from the 3D simulation and the local ratio N_l/f and the steady state temperature from the 2D azimuthally symmetric simulation. Both in the classic and the atmosphere-like configurations, the dominant azimuthal wave number in the baroclinic wave observed is wave 3. In both cases the wave remains relatively uniform in its shape and the phase velocity with which it drifts in an anti-clockwise azimuthal direction. In the atmosphere-like configuration the simulation shows a transition from the wave 3 into a wave 2 after an integration time of about 2.8 h, but the wave 3 recovers again after about 0.7 h. A comparison of the velocity vector fields in figures 2 and 4 shows that in the case of the atmosphere-like configuration the centres of low temperature have a stronger vortex character than in the classic configuration where the jet meanders relatively uniformly between centres of lower and higher temperature. $N^2 \approx 0.33\,(0.64)\,\text{s}^{-2}$, $\chi_r \approx 0.07\,(0.41)$, $\chi_z \approx 0.15\,(0.3)$, $Bu \approx 0.08\,(0.16)$, $Ro_{th} \approx 0.04\,(0.22)$ and $N/f \approx 3.6\,(5)$ are typical values from the 3D simulations of the atmosphere-like configuration (values from the 2D simulations are in parentheses). For comparison, simulations of the classic configuration produce $N^2 \approx 0.12\,(0.14)\,\text{s}^{-2}$, $\chi_r \approx 0.19\,(0.74)$, $\chi_z \approx 0.77\,(0.89)$, $Bu \approx 0.26\,(0.29)$, $Ro_{th} \approx 0.06\,(0.24)$ and $N/f \approx 0.27\,(0.3)$. Though for estimating N^2 and Bu, $\chi_r \sim \chi_z \sim 1$ was assumed, we see that especially in the 3D simulations $\chi_r < 1$ due to the reduction of the baroclinicity during the growth of the baroclinic wave and $\chi_z < 1$ since the process is accompanied by a vertical expansion of the isopycnals (Douglas & Mason 1973) (notice the vertical expansion of the isotherms between figures 5a and 5b). Theoretical considerations on χ_r and χ_z can be found in Hide (1967). Most importantly for our purposes is that the intended increase of the ratio N/f has been achieved with the atmosphere-like configuration, as can be seen in figure 5c. Now at least $N > f$ on average. The Ekman number of the atmosphere-like configuration is about 100 times larger than that of the classic configuration (see table 1). Thus, according to (3.11) and (3.12) the fraction of the total depth taken up by the Ekman layer increases by a factor of about 10 while the fraction of the gap taken up by the inner and outer Stewartson layers increases by a factor of about 5.

10   *S. Borchert, U. Achatz and M. D. Fruman*

4. The gravity-wave signal

4.1. *Simulations*

For the simulation of GWs the grid resolutions used to determine the large scale velocity and temperature fields shown above are too coarse since the spatial scales of the GWs can be assumed to be much smaller than those of the baroclinic waves according to the simulations by Jacoby *et al.* (2011). In addition to increasing the number of grid cells, one may gain further resolution in the azimuthal direction by restricting the simulation to one azimuthal wave length of the dominant baroclinic wave (Williams 1969, 1971), a method also common in simulations of baroclinic waves in the atmosphere (e.g. Simmons & Hoskins 1975). Thus the original 2π-periodicity in azimuthal coordinate was replaced in both configurations, classic and atmosphere-like, by a $2\pi/3$-periodicity. In the case of the atmosphere-like configuration we restrict our investigations to times much earlier than when the wave-3 to wave-2 transition occurred in the coarse simulation. In addition we performed simulations with 2π-periodicity using the same number of grid cells as in case of the $2\pi/3$-periodicity. The results (not shown), although three times coarser resolved in the azimuthal direction, convinced us that the $2\pi/3$-periodic simulations represent the full 2π-periodic flow sufficiently well for this study. The spatial resolutions in the "fine" $2\pi/3$-periodic simulations are listed in table 2. In order to save computing time the fine simulations were initialised with interpolations from a less highly resolved pre-simulation, the specifications of which can be found in the columns labelled "coarse 2" in table 2. Note that in the case of the classic configuration the baroclinic wave cannot be triggered under $2\pi/3$-periodicity. The initial instability is characterised by wave 2 which only after a few minutes undergoes a transition to wave 3. Therefore the pre-simulation was done in the full annulus and a third of it interpolated to initialise the fine simulation. The integration times of the pre-simulations were $2100\,\mathrm{s}$ for the atmosphere-like and $600\,\mathrm{s}$ for the classic configuration. The subsequent simulations on the fine grid lasted for a further $1100\,\mathrm{s}$ in the atmosphere-like and $400\,\mathrm{s}$ in the classic configuration. These times were long enough that any artefacts of the interpolation would have disappeared.

In order to indicate possible GWs, a horizontal cross-section of the horizontal velocity divergence

$$\delta = \boldsymbol{\nabla}_h \cdot \boldsymbol{u} = \frac{1}{r}\left[\frac{\partial u}{\partial \vartheta} + \frac{\partial (rv)}{\partial r}\right] \qquad (4.1)$$

at mid-depth is plotted in figure 6 (e.g. O'Sullivan & Dunkerton 1995). It should be noted that δ contains a balanced part, which affects its suitability as a proxy for GW activity. In the case of a quasi-geostrophic flow, the balanced part of δ can be obtained from the omega equation for the quasi-geostrophic vertical velocity and (3.6d) (e.g. Zhang *et al.* 2000; Viúdez & Dritschel 2006; Plougonven *et al.* 2009; Danioux *et al.* 2012). Subtracting the balanced horizontal divergence from the total would highlight the gravity-wave signal especially clearly. Nevertheless, we assume that the balanced part does not dominate the divergence signal and note that the divergence is still a widely used GW indicator (see e.g. Vanneste 2013; Plougonven & Zhang 2014). The most noticeable structures in the divergence signal are already identifiable with comparable magnitude in the pre-simulation suggesting that they are not merely numerical artefacts of the interpolation. We have also tested whether the divergence signal might be affected by the implicit SGS model ALDM. A repetition of the above simulations using a simple central-difference scheme (e.g. Ferziger & Perić 2008) instead of ALDM to compute the advective fluxes showed no difference in the typical shape, magnitude and other characteristics of the divergence signal (not shown). On the one hand we may conclude from this that the grid resolutions is sufficiently high so that a SGS model is no longer necessary. On the other

hand it shows that the inclusion of ALDM does not adversely affect the GWs in these simulations. Simulations using the grid resolutions "coarse 1" and "coarse 2" in table 2, however, appear to profit from ALDM, since it produces a smoother solution, which more closely resembles the solution of the fine simulations than does using simple central differences (Borchert *et al.* 2014).

In the more atmosphere-like configuration there is a strongly localised signal in the boundary layer region of the inner cylinder, probably consisting of GWs originating from boundary layer instabilities as described by Jacoby *et al.* (2011) and Randriamampianina (2013). In addition one can see spiral-like patterns arranged around the low-pressure centre. A substantial part of these GWs might come from the boundary-layer generated waves since they propagate into the interior of the annular channel as pointed out by Jacoby *et al.* (2011). In the classic configuration the overall picture is comparable. One can see horizontal divergence signals close to the boundary layer of the inner cylinder and unlike in the atmosphere-like configuration band-like horizontal divergence structures following the jet of the baroclinic wave.

The divergence field simulated by our model compares favourably with results from other models. The GWs in both annulus configurations resemble in their spatial structure those observed in simulations of an idealised lifecycle of an unstable baroclinic wave in the atmosphere by O'Sullivan & Dunkerton (1995), Zhang (2004), Plougonven & Snyder (2005) and Plougonven & Snyder (2007). Similar GWs were also observed in simulations of vortex dipoles in a rotating, stratified fluid by Snyder *et al.* (2007, 2009). As was stated by these authors, the GWs are almost stationary with respect to the baroclinic wave or the vortex dipole. We observe the same behaviour in our simulations. The GWs appear to be an inherent feature of the baroclinic wave. In the aforementioned works the GWs are attributed to spontaneous emission from imbalances of the large-scale flow, so a portion of the GWs in the rotating annulus possibly originates from spontaneous GW emission.

It is likely that, regardless of the sources of the GWs, the spatial organisation of the GW field as indicated by the horizontal divergence is primarily determined by the propagation of the waves through the background flow. According to Bühler & McIntyre (2005), Plougonven & Snyder (2005) and Wang *et al.* (2009) the horizontal deformation and vertical shear of the background velocity field appear to have a large impact on the location, orientation and other characteristics of the waves (such as their wavelengths).

4.2. *Analysis*

4.2.1. *Modal decomposition based on linear theory*

An important element in the investigation of GWs in numerical simulations is to test whether the characteristics of the observed structures, assumed to be GWs, are consistent with predictions from linear GW theory (O'Sullivan & Dunkerton 1995; Zhang 2004; Plougonven & Snyder 2007). For this purpose we decompose the flow into small-scale and large-scale parts by means of a moving average. Next, we determine how the energy in the small-scale part of the flow is distributed among the various modes of the linearised governing equations, which shows what part of the small-scale structures of the flow is consistent with the polarisation relations of linear GWs.

The analysis is based on the Boussinesq equations in the formulation (3.6). Expressing the governing equations in Cartesian coordinates, all fields are decomposed into a large-

scale part and small-scale deviations, i.e.

$$\boldsymbol{v} = \boldsymbol{V_0} + \boldsymbol{v'}, \tag{4.2a}$$

$$B = B_0 + B', \tag{4.2b}$$

$$p = P_0 + p', \tag{4.2c}$$

with

$$U_0 = \frac{1}{f}\frac{\partial P_0}{\partial y}, \tag{4.3a}$$

$$V_0 = -\frac{1}{f}\frac{\partial P_0}{\partial x}, \tag{4.3b}$$

$$W_0 = 0, \tag{4.3c}$$

$$B_0 = \frac{\partial P_0}{\partial z}, \tag{4.3d}$$

$$\frac{\partial B_0}{\partial z} = N^2, \tag{4.3e}$$

where U_0, V_0 and W_0 are the velocity components in the x-,y- and z- (i.e. azimuthal, radial, and vertical) directions. Following the standard WKB procedure (e.g. Grimshaw 1975), we assume that U_0, V_0, and N^2 are constants, or rather that their spatial and temporal derivatives are negligible relative to those of the deviations. Writing the linearised Boussinesq equations in terms of the deviations and Fourier-transforming in space and time then yields (e.g. Fritts & Alexander 2003)

$$-\mathrm{i}\hat{\omega}\tilde{u} = -f\tilde{v} - \mathrm{i}k\tilde{p}, \tag{4.4a}$$

$$-\mathrm{i}\hat{\omega}\tilde{v} = f\tilde{u} - \mathrm{i}l\tilde{p}, \tag{4.4b}$$

$$-\mathrm{i}\hat{\omega}\tilde{w} = \tilde{B} - \mathrm{i}m\tilde{p}, \tag{4.4c}$$

$$-\mathrm{i}\hat{\omega}\tilde{B} = -N^2\tilde{w}, \tag{4.4d}$$

$$k\tilde{u} + l\tilde{v} + m\tilde{w} = 0, \tag{4.4e}$$

where k, l, and m are the wave-number components in the x-,y- and z- directions, ω and $\hat{\omega} = \omega - kU_0 - lV_0$ are the frequency and intrinsic frequency, and $\tilde{\phi}$ denotes the Fourier transform of the field ϕ'. The signs of the Coriolis terms in (4.4a) and (4.4b) are reversed compared to those in equation (7) and (8) of Fritts & Alexander (2003) because we changed the usual order of cylindrical coordinates from (r, ϑ, z) to (ϑ, r, z) (a left-handed system) in order to facilitate comparison with the atmosphere (where the zonal direction corresponds to the azimuthal direction in the annulus). In general, the Fourier transforms $\boldsymbol{X} := (\tilde{u}, \tilde{v}, \tilde{w}, \tilde{B})$ can be decomposed into three eigenmodes of the system (4.4). One of these is the geostrophic mode with eigenfrequency

$$\hat{\omega} = \hat{\omega}_1 = 0 \tag{4.5}$$

and structure

$$\boldsymbol{X_1} = \frac{\sqrt{2}fN}{\sqrt{N^2\left(k^2 + l^2\right) + f^2 m^2}}\left(\frac{l}{f}, -\frac{k}{f}, 0, m\right)\mathrm{i}\frac{\tilde{p}}{|\tilde{p}|} =: \boldsymbol{R}. \tag{4.6}$$

The other two are the GW modes with eigenfrequencies

$$\hat{\omega} = \hat{\omega}_{2,3} = \pm\sqrt{\frac{N^2\left(k^2 + l^2\right) + f^2 m^2}{k^2 + l^2 + m^2}} \tag{4.7}$$

and structure

$$
\boldsymbol{X_{2,3}} = \begin{cases} (1, \pm\mathrm{i}, 0, 0)\dfrac{\tilde{u}}{|\tilde{u}|}, & \text{for } k = l = 0 \\[2ex] \dfrac{\tilde{p}/|\tilde{p}|}{\sqrt{k^2 + l^2 + m^2}} \left[\dfrac{m\left(k - \mathrm{i}l\frac{f}{\hat{\omega}}\right)}{\sqrt{k^2 + l^2}}, \dfrac{m\left(l + \mathrm{i}k\frac{f}{\hat{\omega}}\right)}{\sqrt{k^2 + l^2}}, -\sqrt{k^2 + l^2}, \mathrm{i}\dfrac{N^2}{\hat{\omega}}\sqrt{k^2 + l^2} \right], & \text{otherwise} \end{cases}
$$
$$
=: \boldsymbol{G^{\pm}}. \tag{4.8}
$$

The inertial oscillation ($k = l = 0$) is a limiting case, but the case $k = l = m = 0$ is not considered below. The factors (i)$\tilde{p}/|\tilde{p}|$ and $\tilde{u}/|\tilde{u}|$ could equally well be set to unity since they have no bearing on the following analysis. $\boldsymbol{R}$, $\boldsymbol{G^+}$ and $\boldsymbol{G^-}$ form a complete basis of all fields satisfying the continuity equation (4.4e) (Smith & Waleffe 2002; Achatz 2007). The analysis below cannot guarantee that the obtained deviation fields do exactly satisfy (4.4e), so to also allow velocity fields with non-zero divergence we add a fourth basis vector

$$
\boldsymbol{X_4} = \frac{\sqrt{2}}{\sqrt{k^2 + l^2 + m^2}} (k, l, m, 0) =: \boldsymbol{E}, \tag{4.9}
$$

spanning the part of the deviation velocity fields not satisfying (4.4e).
The aforementioned vectors are orthonormal with respect to the energy scalar product

$$
\langle \boldsymbol{X_I}, \boldsymbol{X_J} \rangle := \frac{1}{2}\left(\tilde{u}_I \tilde{u}_J^* + \tilde{v}_I \tilde{v}_J^* + \tilde{w}_I \tilde{w}_J^* + \frac{\tilde{B}_I \tilde{B}_J^*}{N^2} \right), \tag{4.10}
$$

where the asterisk denotes the complex conjugate, i.e. $\langle \boldsymbol{R}, \boldsymbol{R} \rangle = \langle \boldsymbol{G^{\pm}}, \boldsymbol{G^{\pm}} \rangle = \langle \boldsymbol{E}, \boldsymbol{E} \rangle = 1$, and $\langle \boldsymbol{R}, \boldsymbol{G^{\pm}} \rangle = \langle \boldsymbol{G^{\pm}}, \boldsymbol{G^{\mp}} \rangle = \langle \boldsymbol{R}, \boldsymbol{E} \rangle = \langle \boldsymbol{G^{\pm}}, \boldsymbol{E} \rangle = 0$. Now for a given set of wave numbers (k, l, m) the deviations can be expressed as a superposition of the geostrophic and GW modes and the divergent (non-physical) part

$$
\boldsymbol{X} = \varrho\boldsymbol{R} + \gamma^+\boldsymbol{G^+} + \gamma^-\boldsymbol{G^-} + \epsilon\boldsymbol{E}. \tag{4.11}
$$

Up to an irrelevant constant factor the norm corresponding to the scalar product is the sum of the kinetic and available potential energy conserved by the linear Boussinesq equations, and one has

$$
\langle \boldsymbol{X}, \boldsymbol{X} \rangle = \frac{1}{2}\left(\tilde{u}\tilde{u}^* + \tilde{v}\tilde{v}^* + \tilde{w}\tilde{w}^* + \frac{\tilde{B}\tilde{B}^*}{N^2} \right) = |\varrho|^2 + \left|\gamma^+\right|^2 + \left|\gamma^-\right|^2 + |\epsilon|^2. \tag{4.12}
$$

Summing over all wave numbers yields the total energetic contribution from the geostrophic mode, the GWs and the non-physical divergent part (e.g. Achatz 2007)

$$
\mathcal{E}_{geo} = \sum_{k,l,m} |\varrho_{k,l,m}|^2, \tag{4.13a}
$$

$$
\mathcal{E}_{GW} = \sum_{k,l,m} \left|\gamma_{k,l,m}^+\right|^2 + \left|\gamma_{k,l,m}^-\right|^2, \tag{4.13b}
$$

$$
\mathcal{E}_{err} = \sum_{k,l,m} |\epsilon_{k,l,m}|^2. \tag{4.13c}
$$

The large-scale part of the flow is defined by a simple moving average. To each grid-cell with azimuthal, radial and vertical indices i, j, and k we assign a larger averaging box

14   *S. Borchert, U. Achatz and M. D. Fruman*

and determine the large-scale basic field from

$$(\Phi_0)_{i,j,k} = \frac{1}{(2I+1)(2J+1)(2K+1)} \sum_{i'=-I}^{I} \sum_{j'=-J}^{J} \sum_{k'=-K}^{K} \phi_{i+i',j+j',k+k'}, \quad (4.14)$$

where ϕ is one of u, v, and B. Averaging p is not necessary. The azimuthal, radial and vertical extent of the averaging box is chosen to be small enough so that the cylindrical curvature can be neglected. In grid cells where the averaging box extends beyond the radial and vertical annulus bounds, its size is reduced so as to fit in the domain. The local stability is estimated via centred differences using

$$N^2 = \frac{(B_0)_{i,j,k+1} - (B_0)_{i,j,k-1}}{2\Delta z}. \quad (4.15)$$

Within an averaging box we then decompose the fields into mean and deviations and then perform a spatial Fourier transformation with triply periodic boundary conditions. To reduce spectral leakage the amplitude of the deviations $\phi'_{i+i',j+j',k+k'}$ is smoothly reduced to zero towards the boundaries of the averaging box by multiplying it by a window function $\mathfrak{W}_{i',j',k'}$ before applying the Fourier transform. Here we make use of a Tukey window (Harris 1978)

$$\mathfrak{W}_{i',j',k'} = \mathfrak{w}_I(i')\mathfrak{w}_J(j')\mathfrak{w}_K(k'), \quad (4.16)$$

where

$$\mathfrak{w}_I(i') = \begin{cases} \frac{1}{2}\left\{1 + \cos\left[\frac{\pi(-i'-\beta I)}{(1-\beta)I}\right]\right\}, & \text{for } i' < -\beta I \\ 1, & \text{for } -\beta I \leqslant i' \leqslant \beta I, \\ \frac{1}{2}\left\{1 + \cos\left[\frac{\pi(i'-\beta I)}{(1-\beta)I}\right]\right\}, & \text{for } i' > \beta I \end{cases} \quad (4.17)$$

with $\beta = 3/4$, and analogous definitions for $\mathfrak{w}_J(j')$ and $\mathfrak{w}_K(k')$. The Fourier analysis yields for each possible wavenumber combination (k,l,m) the deviation Fourier transforms $\boldsymbol{X}$. We then determine, from the wavenumbers and from f and N, the four basis vectors $\boldsymbol{R}$, $\boldsymbol{G}^+$, $\boldsymbol{G}^-$, and $\boldsymbol{E}$. Projecting $\boldsymbol{X}$ onto these yields the expansion coefficients ϱ, γ^+, γ^-, and ϵ which are finally used to determine the energetic contributions (4.13). This procedure is done grid-cell by grid cell, yielding a spatially varying decomposition of the energy.

Figure 7 shows the analysis results for the snapshot of the annulus flow shown in figure 6. We have used an averaging and analysis box of size $I = J = K = 25$ in the case of the classic configuration and $I = K = 20$, $J = 30$ for the atmosphere-like configuration. In both configurations the energy contained in the geostrophic mode $\mathcal{E}_{geo}$ is of comparable magnitude to the energy of the two GW modes $\mathcal{E}_{GW}$. The energy in the non-physical part of the velocity field $\mathcal{E}_{err}$ is about an order-of magnitude smaller (not shown). The classic configuration has highest energy values of the geostrophic mode in the region of the jet, where the temperature and velocity fields vary relatively strongly (compare figure 2). The energy of the GW modes $\mathcal{E}_{GW}$ has its highest values in the jet region as well. This coincides with the pattern of the horizontal velocity divergence (figure 6a). For the atmosphere-like configuration both, $\mathcal{E}_{geo}$ and $\mathcal{E}_{GW}$ have their maximum close to the low-pressure centre (compare figure 6b). This might likewise be associated with stronger variations of temperature and velocity fields in this region (compare figure 4). The energy signal of the GW modes coincides with the signal of the horizontal velocity divergence also in this case (figure 6b). Note that the boundary layer regions lie outside of the analysed sub-region since in our implementation the analysis box cannot cross the solid walls of

the annulus (compare to figure 7a, b). Although we claim that these results are a useful contribution to the collection of indicators for GW activity in the annulus experiment, it should be acknowledged that the analysis is not unambiguous due to the freedom in the choice of the averaging volume and the simplifications involved in the linearisation of the governing equations. So some caution is required in the interpretation of these results. It is not surprising that all energies increase with increasing box size, but in our tests the ratio of the various energies to the total energy depends only slightly on the box size. Thus this analysis is assumed to give (at least) information on the relative energy distribution between the geostrophic mode and the GWs, which in our case suggests that GWs contribute significantly to the small-scale structures of the flow.

The decomposition of the flow into a smoothed large-scale part and the small-scale deviations using a moving average has to be distinguished from the decomposition into balanced and unbalanced parts, which is a common method to identify GWs, e.g., Warn *et al.* (1995); Zhang *et al.* (2000); Snyder *et al.* (2009); Wang & Zhang (2010). In those works, diagnostic relations are used to determine the GW-free balanced (large-scale) part of the flow (geostrophic balance is a simple example). The deviation of the flow from the balanced part is the unbalanced part, which is assumed to contain the GWs. Although, the analysis presented here is not based on the decomposition into balanced and unbalanced parts, it might be used in the future to investigate a question which has attracted some interest in past works, namely that of the dependence of the energy in the small-scale structures on the Rossby number. In a simplified model of spontaneous GW emission, it has been shown analytically using exponential asymptotics that in the limit $Ro \ll 1$ the amplitude of the GWs is exponentially small in the Rossby number, more precisely proportional to $Ro^{-1/2} \exp(-\alpha/Ro)$ (Vanneste & Yavneh 2004). Numerical simulations of vortex dipoles, on the other hand, suggest a power-law dependence Ro^{β} with typical values of $\beta \approx 4$ (Snyder *et al.* 2007) or $\beta \approx 6$ (Wang *et al.* 2009) for the considered Rossby number range. Meanwhile, laboratory observations from a rotating two-layer annulus found the amplitude of small-scale waves to vary linearly with the Rossby number in the considered range (Williams *et al.* 2008). For the differentially heated rotating annulus it would be necessary to investigate a large number of experiments with different parameters to cover a large enough range of the Rossby number. The thermal Rossby number (3.8) might be used as reference point to find suitable parameters, while the Rossby number defined by characteristic velocity and length scales identified in the actual flow would be used for comparison with the aforementioned works. Note that instead of yielding the absolute dependence of the energy in the small scale structures on the Rossby number, the analysis method presented in this section is only suitable for obtaining the relative change in energy as Ro changes.

5. Summary and discussion

Determining the importance of large-scale balanced flow as a source of GWs in the atmosphere is one of the major challenges facing modellers wishing to improve the parameterisation of GWs in weather prediction and climate simulation. Given the inherent difficulty of using data from direct atmospheric measurements for validating and advancing theory, it would be valuable to have complementary laboratory experiments available where an elusive process like spontaneous GW emission can be investigated in a controlled and systematic way. One such experiment is the differentially heated rotating annulus (Hide 1958), a classic laboratory analogue for mid-latitude atmospheric flows. Indications of GW activity in the rotating annulus have been reported, but either a two-layer variant of the experiment was used (Williams *et al.* 2005) or the waves

were attributable to boundary layer instabilities (Jacoby *et al.* 2011; Randriamampianina 2013). The purpose of the present modelling study is to investigate whether and how a rotating-annulus experiment with continuous stratification might be designed to be useful for the investigation of spontaneous GW emission. Our tool is a new numerical model of the differentially heated rotating annulus (Borchert *et al.* 2014) that integrates the Boussinesq equations using a finite-volume discretisation with the implicit subgrid-scale parameterisation developed by Hickel *et al.* (2006).

In the classic configuration of the annulus experiment the ratio N/f of the mean Brunt-Väisälä frequency N to the inertial frequency f is less than unity (in the regime of baroclinic instability) unlike in the real atmosphere where $N/f \sim 100$. These two frequencies define the range of intrinsic frequencies for GWs, with horizontally propagating waves having frequencies closer to N and vertically propagating waves frequencies closer to f. The fact that in the atmosphere, the former are very high frequency and the latter very low frequency is central to their importance to the large-scale circulation and to the problems they pose to modellers. If the annulus experiment is to serve as an analogue for GW processes in the atmosphere, it is therefore desirable to design it in such a way that $N/f > 1$ and the "ordering" is preserved. Without differential heating at the top and bottom boundaries (the set-up suggested by Miller & Fowlis (1986)) the only way to increase N/f is by increasing the temperature difference between the inner and outer walls, by decreasing the fluid depth, and by decreasing the rotation rate. Care has to be taken that this is done in such a way that baroclinic instability is still active, as it provides the large-scale wave from which GWs are to be radiated. Quasi-geostrophic theory (Charney 1948) in the approximation of Eady (1949) has been used to identify parameters that at once maximise N/f, preserve baroclinic instability, and remain within realistic limits for eventual implementation in the laboratory. We found a wide and shallow, slowly rotating annulus with comparatively large lateral temperature difference to be the configuration of choice. In one such configuration with inner and outer radii $a = 20\,\mathrm{cm}$ and $b = 70\,\mathrm{cm}$, fluid depth $d = 4\,\mathrm{cm}$, temperature difference $T_b - T_a = 30\,\mathrm{K}$ and angular velocity $\Omega = 0.08\,\mathrm{rad/s}$ (0.76 rpm), our numerical model predicts $N/f \sim 4$, slightly less than our theoretical expectation. We have performed simulations with both this more atmosphere-like configuration and a classic configuration, with cylinder radii $a = 4.5\,\mathrm{cm}$ and $b = 12\,\mathrm{cm}$, fluid depth $d = 13.5\,\mathrm{cm}$, temperature difference $T_b - T_a = 8\,\mathrm{K}$ and angular velocity $\Omega = 0.63\,\mathrm{rad/s}$ (6 rpm). These values are very close to those used in a laboratory experiment by Harlander *et al.* (2011). In this configuration we observe $N/f \sim 0.3$.

Clear signals are observed in the horizontal divergence field, a likely indicator of GW activity, in both configurations, both close to the inner boundary and within the baroclinic wave. Within the baroclinic wave, they take the form of small-scale spiral patterns in the atmosphere-like configuration and band-like patterns in the classic configuration. Especially in the first configuration, the structures are reminiscent of the spontaneously emitted GWs observed in simulations of atmospheric baroclinic waves (e.g. O'Sullivan & Dunkerton 1995). Modal decomposition based on linear theory suggests that GWs contribute significantly to the small-scale energy in regions where the horizontal-divergence structures are found. A substantial part of the GW signal seems to originate from a localised instability in the boundary layer at the inner cylinder, similar to those described by Jacoby *et al.* (2011) and Randriamampianina (2013).

In a future work we will address the problem of finding further indications which underpin the assumption that a part of the GWs observed in the simulations of the rotating annulus originates from spontaneous GW emission. In this context, we hope to clarify how significant this GW forcing is in comparison to the boundary layer instabilities. Preliminary results already indicate a clear forcing of horizontal divergence by the

geostrophically and hydrostatically balanced flow (not shown), indicating a local GW source apart from boundary layer instabilities. The approaches of Snyder *et al.* (2009) and Wang & Zhang (2010) can be further promising tools for this investigation. They linearised the governing equations about a balanced state (either a quasi-geostrophic or a nonlinear balance), obtaining equations for the small-scale deviations forced by the residual tendency of the balanced flow. Vortex dipole simulations showed good qualitative agreement between the forced linear solution and the GWs from the fully nonlinear simulations. Wang & Zhang (2010) showed that the forcing of the relative vorticity deviation contributes most to the spontaneously emitted GWs in their test case.

Although a proof of spontaneous GW emission in the differentially heated rotating annulus is still pending and boundary-layer effects are considerable, even in our wider, atmosphere-like annulus simulations, we hope that our results so far will provide a guideline, or at least motivation, to colleagues in the laboratory to address spontaneous GW emission in new configurations of the differentially heated rotating annulus.

Acknowledgements

REFERENCES

ACHATZ, U. 2007 Modal and nonmodal perturbations of monochromatic high-frequency gravity waves: primary nonlinear dynamics. *J. Atmos. Sci.* **64**, 1977–1994.

AFANASYEV, Y. 2003 Spontaneous emission of gravity waves by interacting vortex dipoles in a stratified fluid: laboratory experiments. *Geophys. Astrophys. Fluid Dyn.* **97**, 79–95.

ALEXANDER, M. J., GELLER, M., MCLANDRESS, C., POLAVARAPU, S., PREUSSE, P., SASSI, F., SATO, K., ECKERMANN, S., ERN, M., HERTZOG, A., KAWATANI, Y., PULIDO, M., SHAW, T. A., SIGMOND, M., , VINCENT, R. & WATANABE, S. 2010 Recent developments in gravity-wave effects in climate models and the global distribution of gravity-wave momentum flux from observations and models. *Quart. J. R. Met. Soc.* **136**, 1103–1124.

ALLEN, J. S. 1972 Upwelling of a stratified fluid in a rotating annulus: steady state. Part 1. Linear theory. *J. Fluid Mech.* **56**, 429–445.

ARAKAWA, A. & LAMB, V. R. 1977 Computational design of the basic dynamical processes of the UCLA general circulation model. *Methods in Computational Physics* **17**, 173–265.

BARCILON, V. & PEDLOSKY, J. 1967*a* Linear theory of rotating stratified fluid motions. *J. Fluid Mech.* **29**, 1–16.

BARCILON, V. & PEDLOSKY, J. 1967*b* A unified linear theory of homogeneous and stratified rotating fluids. *J. Fluid Mech.* **29**, 609–621.

BASTIN, M. E. & READ, P. L. 1998 Experiments on the structure of baroclinic waves and zonal jets in an internally heated, rotating, cylinder of fluid. *Phys. Fluids* **10** (2), 374–389.

BERES, J. H., ALEXANDER, M. J. & HOLTON, J. R. 2004 A method of specifying the gravity wave spectrum above convection based on latent heating properties and background wind. *J. Atmos. Sci.* **61**, 324–337.

BERES, J. H., GARCIA, R. R., BOVILLE, B. A. & SASSI, F. 2005 Implementation of a gravity wave source spectrum parameterization dependent on the properties of convection in the Whole Atmosphere Community Climate Model (WACCM). *J. Geophys. Res.* **110**, D10108.

BORCHERT, S., ACHATZ, U., REMMLER, S., HICKEL, S., HARLANDER, U., VINCZE, M., ALEXANDROV, K. D., RIEPER, F., HEPPELMANN, T. & DOLAPTCHIEV, S. I. 2014 Finite-

18   *S. Borchert, U. Achatz and M. D. Fruman*

volume models with implicit subgrid-scale parameterization for the differentially heated rotating annulus. *Meteorol. Z.* p. submitted.

BÜHLER, O. & MCINTYRE, M. E. 2005 Wave capture and wave-vortex duality. *J. Fluid Mech.* **534**, 67–95.

CHARNEY, J. G. 1948 On the scale of atmospheric motions. *Geofys. Publ. Oslo* **17**, 1–17.

CHUN, H.-Y. & BAIK, J.-J. 1998 Momentum flux by thermally induced internal gravity waves and its approximation for large-scale models. *J. Atmos. Sci.* **55**, 3299–3310.

CHUN, H.-Y., SONG, I.-S., BAIK, J.-J. & KIM, Y.-J. 2004 Impact of a convectively forced gravity wave drag parameterization in NCAR CCM3. *J. Climate* **17**, 3530–3547.

CLAPHAM, C. & NICHOLSON, J. 2009 *The Concise Oxford Dictionary of Mathematics*, 4th edn. Oxford University Press.

DANIOUX, E., VANNESTE, J., KLEIN, P. & SASAKI, H. 2012 Spontaneous inertia-gravity-wave generation by surface-intensified turbulence. *J. Fluid Mech.* **699**, 153–173.

DOUGLAS, H. A. & MASON, P. J. 1973 Thermal convection in a large rotating fluid annulus: some effects of varying the aspect ratio. *J. Atmos. Sci.* **30**, 1124–1134.

EADY, E. T. 1949 Long waves and cyclone waves. *Tellus* **1**, 33–52.

ESLER, J.G. & POLVANI, L.M. 2004 Kelvin-helmholtz instability of potential vorticity layers: a route to mixing. *J. Atmos. Sci.* **61**, 1392–1405.

FARNELL, L. & PLUMB, R. A. 1975 Numerical integration of flow in a rotating annulus I: axisymmetric model. *Tech. Rep..* Geophysical Fluid Dynamics Laboratory, UK, Meteorological Office.

FARNELL, L. & PLUMB, R. A. 1976 Numerical integration of flow in a rotating annulus II: three dimensional model. *Tech. Rep..* Geophysical Fluid Dynamics Laboratory, UK, Meteorological Office.

FERZIGER, J. H. & PERIĆ, M. 2008 *Numerische Strömungsmechanik* (Title of the english edition: *Computational methods for fluid dynamics*). Berlin: Springer-Verlag.

FORD, R. 1994*a* Gravity wave radiation from vortex trains in rotating shallow water. *J. Fluid Mech.* **281**, 81–118.

FORD, R. 1994*b* The instability of an axisymmetric vortex with monotonic potential vorticity in rotating shallow water. *J. Fluid Mech.* **280**, 303–334.

FORD, R. 1994*c* The response of a rotating ellipse of uniform potential vorticity to gravity wave radiation. *Phys. Fluids* **6**, 3694–3704.

FRITTS, D. C. & ALEXANDER, M. J. 2003 Gravity wave dynamics and effects in the middle atmosphere. *Rev. Geophys.* **41** (1), 1003.

FRITTS, D. C. & LUO, Z. 1992 Gravity wave excitation by geostrophic adjustment of the jet stream. Part I: two-dimensional forcing. *J. Atmos. Sci.* **49**, 681–697.

GERMANO, M., PIOMELLI, U., MOIN, P. & CABOT, W. H. 1991 A dynamic subgrid-scale eddy viscosity model. *Phys. Fluids* **A 3**, 17601765.

GILL, A. E. 1982 *Atmosphere-ocean dynamics*. New York: Academic Press, Inc.

GRIMSHAW, R. 1975 Internal gravity waves: critical layer absorption in a rotating fluid. *J. Fluid Mech.* **70**, 287–304.

GUEST, F. M., REEDER, M. J., MARKS, C. J. & KAROLY, D. J. 2000 Inertia-gravity waves observed in the lower stratosphere over Macquarie Island. *J. Atmos. Sci.* **57**, 737–752.

HARLANDER, U., VON LARCHER, TH., WANG, Y. & EGBERS, CH. 2011 PIV- and LDV-measurements of baroclinic wave interactions in a thermally driven rotating annulus. *Exp. Fluids* **51** (1), 37–49.

HARRIS, F. J. 1978 On the use of windows for harmonic analysis with the discrete fourier transform. *Proceedings of the IEEE* **66**, 51–83.

HATHAWAY, D. H. & FOWLIS, W. W. 1986 Flow regimes in a shallow rotating cylindrical annulus with temperature gradients imposed on the horizontal boundaries. *J. Fluid Mech.* **172**, 401–418.

HICKEL, S. & ADAMS, N. A. 2007 On implicit subgrid-scale modeling in wall-bounded flows. *Phys. Fluids* **19**, 105106.

HICKEL, S. & ADAMS, N. A. 2008 Implicit LES applied to zero-pressure-gradient and adverse-pressure-gradient boundary-layer turbulence. *Int. J. Heat Fluid Flow* **29**, 626–639.

HICKEL, S., ADAMS, N. A. & DOMARADZKI, J. A. 2006 An adaptive local deconvolution method for implicit LES. *J. Comp. Phys.* **213**, 413–436.

HICKEL, S., KEMPE, T. & ADAMS, N. A. 2008 Implicit large-eddy simulation applied to turbulent channel flow with periodic constrictions. *Theor. Comput. Fluid Dyn.* **22**, 227–242.

HIDE, R. 1958 An experimental study of thermal convection in a rotating liquid. *Phil. Trans. Roy. Soc. Lond.* **A250**, 441–478.

HIDE, R. 1967 Theory of axisymmetric thermal convection in a rotating fluid annulus. *Phys. Fluids* **10** (1), 56–68.

HIDE, R. & MASON, P. J. 1975 Sloping convection in a rotating fluid. *Adv. Phys.* **24** (1), 47–100.

HIGNETT, P., WHITE, A. A., CARTER, R. D., JACKSON, W. D. N. & SMALL, R. M. 1985 A comparison of laboratory measurements and numerical simulations of baroclinic wave flows in a rotating cylindrical annulus. *Quart. J. R. Met. Soc.* **111**, 131–154.

JACOBY, T. N. L., READ, P. L., WILLIAMS, P. D. & YOUNG, R. M. B. 2011 Generation of inertia-gravity waves in the rotating thermal annulus by a localised boundary layer instability. *Geophys. Astrophys. Fluid Dyn.* **105**, 161–181.

JAMES, I. N., JONAS, P. R. & FARNELL, L. 1981 A combined laboratory and numerical study of fully developed steady baroclinic waves in a cylindrical annulus. *Quart. J. R. Met. Soc.* **107**, 51–78.

KIM, Y.-J., ECKERMANN, S. D. & CHUN, H.-Y. 2003 An overview of the past, present and future of gravity-wav drag parametrization for numerical climate and weather prediction models. *Atmos.-Ocean* **41**, 65–98.

KWAK, H. S. & HYUN, J. M. 1992 Baroclinic waves in a shallow rotating annulus with temperature gradients imposed on the horizontal boundaries. *Geophys. Astrophys. Fluid Dyn.* **66**, 1–23.

LIGHTHILL, M. J. 1952 On sound generated aerodynamically. I. General theory. *Proc. Roy. Soc. Lond.* **211**, 564–587.

LOVEGROVE, A. F., READ, P. L. & RICHARDS, C. J. 1999 Generation of inertia-gravity waves by a time-dependent baroclinic wave in the laboratory. *Phys. Chem. Earth (B)* **24**, 455–460.

LOVEGROVE, A. F., READ, P. L. & RICHARDS, C. J. 2000 Generation of inertia-gravity waves in a baroclinically unstable fluid. *Quart. J. R. Met. Soc.* **126**, 3233–3254.

LUO, Z. & FRITTS, D. C. 1993 Gravity-wave excitation by geostrophic adjustment of the jet stream. Part II: three-dimensional forcing. *J. Atmos. Sci.* **50**, 104–115.

MCFARLANE, N. A. 1987 The effect of orographically excited gravity wave drag on the general circulation of the lower stratosphere and troposphere. *J. Atmos. Sci.* **44**, 1775–1800.

MEISTER, A. 2011 *Numerik linearer Gleichungssysteme. Eine Einführung in moderne Verfahren. (Numerical methods for linear systems of equations. An introduction to modern methods.).* Wiesbaden: Vieweg+Teubner.

MILLER, T. L. & FOWLIS, W. W. 1986 Laboratory experiments in a baroclinic annulus with heating and cooling on the horizontal boundaries. *Geophys. Astrophys. Fluid Dyn.* **34**, 283–300.

MÜLLER, P., HOLLOWAY, G., HENYEY, F. & POMPHREY, N. 1986 Nonlinear interactions among internal gravity waves. *Rev. Geophys.* **24**, 493–536.

O'SULLIVAN, D. & DUNKERTON, T. J. 1995 Generation of inertia-gravity waves in a simulated life cycle of baroclinic instability. *J. Atmos. Sci.* **52**, 3695–3716.

PALMER, T. N., SHUTTS, G. J. & SWINBANK, R. 1986 Alleviation of a systematic westerly bias in general circulation and numerical weather prediction models through an orographic gravity wave drag parametrization. *Quart. J. R. Met. Soc.* **112**, 1001–1039.

PAVELIN, E., WHITEWAY, J. A. & VAUGHAN, G. 2001 Observation of gravity wave generation and breaking in the lowermost stratosphere. *J. Geophys. Res.* **106**, 5173–5179.

PLOUGONVEN, R. & SNYDER, C. 2005 Gravity waves excited by jets: propagation versus generation. *Geophys. Res. Lett.* **32**, L18802.

PLOUGONVEN, R. & SNYDER, C. 2007 Inertia-gravity waves spontaneously generated by jets and fronts. Part I: different baroclinic life cycles. *J. Atmos. Sci.* **64**, 2502–2520.

PLOUGONVEN, R., SNYDER, C. & ZHANG, F. 2009 Comments on "Application of the Lighthill–Ford theory of spontaneous imbalance to clear-air turbulence forecasting". *J. Atmos. Sci.* **66**, 2506–2510.

PLOUGONVEN, R., TEITELBAUM, H. & ZEITLIN, V. 2003 Inertia gravity wave generation by the tropospheric midlatitude jet as given by the Fronts and Atlantic Storm-Track Experiment radio soundings. *J. Geophys. Res.* **108**, 4686.

20   *S. Borchert, U. Achatz and M. D. Fruman*

PLOUGONVEN, R. & ZHANG, F. 2014 Internal gravity waves from atmospheric jets and fronts. *Rev. Geophys.* **52**, 33–76.

RANDRIAMAMPIANINA, A. 2013 Caractéristiques d'ondes d'inertie gravité dans une cavité baro-cline (Inertia gravity waves characteristics within a baroclinic cavity). *C. R. Mecanique* **341**, 547–552.

READ, P. L., LEWIS, S. R. & HIDE, R. 1997 Laboratory and numerical studies of baroclinic waves in an internally heated rotating fluid annulus: a case of wave\vortex duality? *J. Fluid Mech.* **337**, 155–191.

REMMLER, S. & HICKEL, S. 2012 Direct and large eddy simulation of stratified turbulence. *Int. J. Heat Fluid Flow* **35**, 13–24.

RICHTER, J. H., SASSI, F. & GARCIA, R. R. 2010 Toward a physically based gravity wave source parameterization in a general circulation model. *J. Atmos. Sci.* **67**, 136–156.

RIEHL, H. & FULTZ, D. 1957 Jet stream and long waves in a steady rotating-dishpan experiment: structure of the circulation. *Quart. J. R. Met. Soc.* **83**, 215–231.

RIEPER, F., HICKEL, S. & ACHATZ, U. 2013 A conservative integration of the pseudo-incompressible equations with implicit turbulence parameterization. *Mon. Weather Rev.* **141**, 861–886.

ROSSBY, C.-G. 1926 On the solution of problems of atmospheric motion by means of model experiments. *Mon. Weather Rev.* **54** (6), 237–240.

ROSSBY, C.-G. 1938 On the mutual adjustment of pressure and velocity distributions in certain simple current systems, ii. *J. Mar. Res.* **2**, 239–263.

SATO, K., WATANABE, S., KAWATANI, Y., TOMIKAWA, Y., MIYAZAKI, K. & TAKAHASHI, M. 2009 On the origins of mesospheric gravity waves. *Geophys. Res. Lett.* **36**, L19801.

SIMMONS, A. J. & HOSKINS, B. J. 1975 A comparison of spectral and finite-difference simulations of a growing baroclinic wave. *Quart. J. R. Met. Soc.* **101**, 551–565.

SMITH, L. M. & WALEFFE, F. 2002 Generation of slow large scales in forced rotating stratified turbulence. *J. Fluid Mech.* **451**, 145–168.

SNYDER, C., MURAKI, D. J., PLOUGONVEN, R. & ZHANG, F. 2007 Inertia-gravity waves generated within a dipole vortex. *J. Atmos. Sci.* **64**, 4417–4431.

SNYDER, C., PLOUGONVEN, R. & MURAKI, D. J. 2009 Mechanisms for spontaneous gravity wave generation within a dipole vortex. *J. Atmos. Sci.* **66**, 3464–3478.

SONG, I.-S. & CHUN, H.-Y. 2008 A Lagrangian spectral parameterization of gravity wave drag induced by cumulus convection. *J. Atmos. Sci.* **65**, 1204–1224.

UCCELLINI, L. W. & KOCH, S. E. 1987 The synoptic setting and possible energy sources for mesoscale wave disturbances. *Mon. Weather Rev.* **115**, 721–729.

VALLIS, G. K. 2006 *Atmospheric and oceanic fluid dynamics: fundamentals and large-scale circulation.* New York: Cambridge University Press.

VANNESTE, J. 2013 Balance and spontaneous wave generation in geophysical flows. *Ann. Rev. Fluid Mech.* **45**, 147–172.

VANNESTE, J. & YAVNEH, I. 2004 Exponentially small inertia-gravity waves and the breakdown of quasigeostrophic balance. *J. Atmos. Sci.* **61**, 211–223.

VEREIN DEUTSCHER INGENIEURE, VDI-GESELLSCHAFT VERFAHRENSTECHNIK & CHEMIEIN-GENIEURWESEN (GVC), ed. 2006 *VDI-Wärmeatlas*, 10th edn. Berlin: Springer-Verlag.

VIÚDEZ, Á. & DRITSCHEL, D. G. 2006 Spontaneous generation of inertia-gravity wave packets by balanced geophysical flows. *J. Fluid Mech.* **553**, 107–117.

VON LARCHER, TH. & EGBERS, CH. 2005 Experiments on transitions of baroclinic waves in a differentially heated rotating annulus. *Nonlin. Processes Geophys.* **12**, 1033–1041.

WANG, S. & ZHANG, F. 2010 Source of gravity waves within a vortex-dipole jet revealed by a linear model. *J. Atmos. Sci.* **67**, 1438–1455.

WANG, S., ZHANG, F. & SNYDER, C. 2009 Generation and propagation of inertia-gravity waves from vortex dipoles and jets. *J. Atmos. Sci.* **66**, 1294–1314.

WARN, T., BOKHOVE, O., SHEPHERD, T. G. & VALLIS, G. K. 1995 Rossby number expansions, slaving principles, and balance dynamics. *Quart. J. R. Met. Soc.* **121**, 723–739.

WILLIAMS, G. P. 1967 Thermal convection in a rotating fluid annulus: part 1. The basic axisymmetric flow. *J. Atmos. Sci.* **24**, 144–161.

WILLIAMS, G. P. 1969 Numerical integration of the three-dimensional Navier-Stokes equations for incompressible flow. *J. Fluid Mech.* **37**, 727–750.

WILLIAMS, G. P. 1971 Baroclinic annulus waves. *J. Fluid Mech.* **49**, 417–449.

WILLIAMS, P. D., HAINE, T. W. N. & READ, P. L. 2005 On the generation mechanisms of short-scale unbalanced modes in rotating two-layer flows with vertical shear. *J. Fluid Mech.* **528**, 1–22.

WILLIAMS, P. D., HAINE, T. W. N. & READ, P. L. 2008 Inertia-gravity waves emitted from balanced flow: observations, properties, and consequences. *J. Atmos. Sci.* **65**, 3543–3556.

WILLIAMS, P. D., READ, P. L. & HAINE, T. W. N. 2003 Spontaneous generation and impact of inertia-gravity waves in a stratified, two-layer shear flow. *Geophys. Res. Lett.* **30**, 2255.

WILLIAMSON, J. H. 1980 Low-storage Runge-Kutta schemes. *J. Comp. Phys.* **35**, 48–56.

ZHANG, F. 2004 Generation of mesoscale gravity waves in upper-tropospheric jet–front systems. *J. Atmos. Sci.* **61**, 440–457.

ZHANG, F., KOCH, S. E., DAVIS, C. A. & KAPLAN, M. L. 2000 A survey of unbalanced flow diagnostics and their application. *Adv. Atmos. Sci.* **17**, 165–183.

22   *S. Borchert, U. Achatz and M. D. Fruman*

	classic configuration	atmosphere-like configuration
- inner radius, a:	4.5 cm	20 cm
- outer radius, b:	12 cm	70 cm
- fluid depth, d:	13.5 cm	4 cm
- inner wall temperature, T_a:	24 °C	15 °C
- outer wall temperature, T_b:	32 °C	45 °C
- angular velocity, Ω:	0.63 rad/s (6 rpm)	0.08 rad/s (0.76 rpm)
- working fluid:	water	water
- ρ_1:	$-2.765 \times 10^{-4}\,1/K$	$-2.923 \times 10^{-4}\,1/K$
- ρ_2:	$-3.915 \times 10^{-6}\,1/K^2$	$-3.917 \times 10^{-6}\,1/K^2$
- ν_0:	$8.543 \times 10^{-3}\,cm^2/s$	$8.160 \times 10^{-3}\,cm^2/s$
- ν_1:	$-2.297 \times 10^{-2}\,1/K$	$-2.292 \times 10^{-2}\,1/K$
- ν_2:	$2.692 \times 10^{-4}\,1/K^2$	$2.819 \times 10^{-4}\,1/K^2$
- κ_0:	$1.469 \times 10^{-3}\,cm^2/s$	$1.477 \times 10^{-3}\,cm^2/s$
- κ_1:	$2.824 \times 10^{-3}\,1/K$	$2.758 \times 10^{-3}\,1/K$
- κ_2:	$-1.266 \times 10^{-5}\,1/K^2$	$-1.259 \times 10^{-5}\,1/K^2$
- Ekman number, Ek:	7×10^{-5}	6×10^{-3}
- Ekman layer thickness, δ_E:	0.12 cm	0.32 cm
- Stewartson layer thickness, δ_S:	0.32 cm	9.27 cm
- thermal boundary layer thickness, δ_T:	0.09 cm	0.05 cm

TABLE 1. Physical parameters and derived quantities for a classic annulus configuration comparable to those used by Harlander *et al.* (2011) and a more atmosphere-like configuration.

	classic configuration			atmosphere-like configuration		
	coarse 1	coarse 2	fine	coarse 1	coarse 2	fine
- number of azimuthal grid cells, N_ϑ:	60	90	160	80	80	160
- — radial — , N_r:	40	45	90	80	80	160
- — vertical — , N_z:	50	80	160	30	30	90
- azimuthal width of simulated periodic sector:	2π rad	2π rad	$2\pi/3$ rad	2π rad	$2\pi/3$ rad	$2\pi/3$ rad
- integration time t_{2D} of 2D model to reach steady state:	10800 s	10800 s	-	36000 s	36000 s	-
- max. amplitude δT_{pert} of initial temperature perturbations, in units of $|T_b - T_a|$:	0.03	0.03	-	0.01	0.01	-

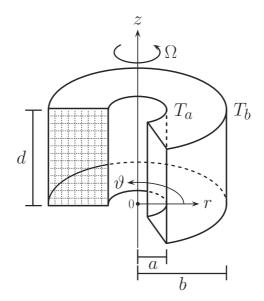TABLE 2. Parameters of the numerical model.

FIGURE 1. Schematic view of the differentially heated rotating annulus with a sector removed to indicate the cell walls of the regular, cylindrical finite-volume grid (dotted lines).
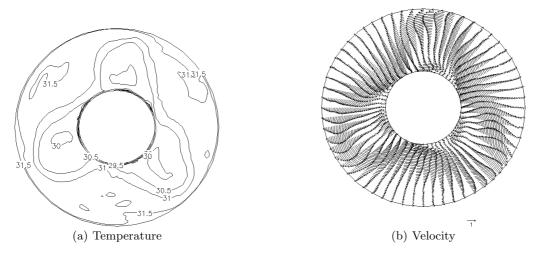

(a) Temperature

(b) Velocity

FIGURE 2. Horizontal cross section of (a) the temperature field in °C, contour interval 0.5 °C simulated for a classic annulus configuration at height $z = 0.74\,d = 10\,\mathrm{cm}$ and time $t = 2700\,\mathrm{s}$ after the seeding of baroclinic instability by a random temperature perturbation, and (b) the corresponding horizontal velocity vector field in cm/s.

(a) 2D: Temperature   (b) 3D: Temperature   (c) 3D: N_l/f
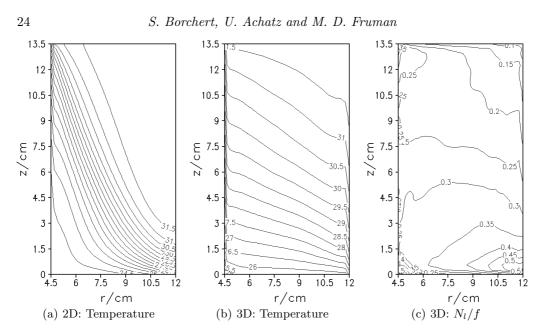
FIGURE 3. (a) Azimuthally symmetric solution for the temperature field from a simulation in the classic annulus configuration. Also shown are the vertical cross-section of (b) the azimuthal-mean temperature and (c) the local ratio N_l/f from the same full 3D simulation as shown in figure 2. The contour interval for the temperature plots is 0.5 °C. The isolines of N_l/f have the contour interval 0.05.
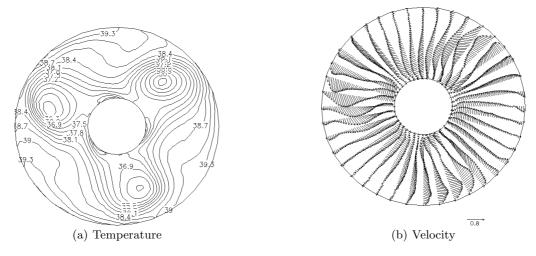

(a) Temperature   (b) Velocity

FIGURE 4. As figure 2, but now for the more atmosphere-like annulus configuration. The plots are at height $z = d/2 = 2$ cm, and time $t = 3600$ s. Contour interval of the isotherms in the left panel is 0.3 °C.
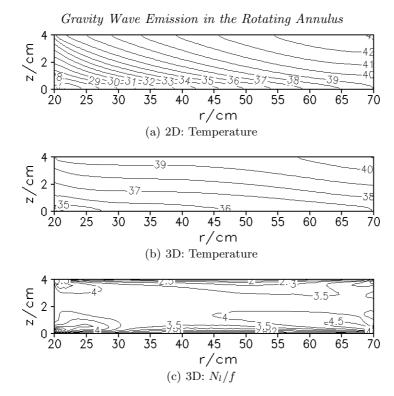
(a) 2D: Temperature

(b) 3D: Temperature

(c) 3D: N_l/f

FIGURE 5. As in figure 3, but now for the atmosphere-like configuration. The contour interval is $1\,^\circ$C for both temperature plots and 0.5 for N_l/f.
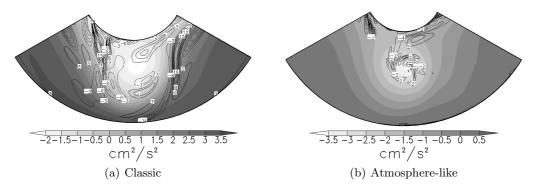

(a) Classic

(b) Atmosphere-like

FIGURE 6. Pressure field (grey scale) and contour lines of the horizontal velocity divergence $\delta = \boldsymbol{\nabla}_h \cdot \boldsymbol{u}$ (a) δ in $10^{-2}\,\mathrm{s}^{-1}$ for the classic configuration at height $z = 0.74 \times d = 10\,\mathrm{cm}$ and time $t = 1000\,\mathrm{s}$ after seeding the baroclinic instability. The contour interval of δ is $3 \times 10^{-2}\,\mathrm{s}^{-1}$. (b) δ in $10^{-2}\,\mathrm{s}^{-1}$ for the atmosphere-like configuration at a height of $z = d/2 = 2\,\mathrm{cm}$ and at time $t = 3200\,\mathrm{s}$, with a contour interval of $2 \times 10^{-2}\,\mathrm{s}^{-1}$ for δ.

(a) Classic: geostrophic   (b) Atmosphere-like: geostrophic

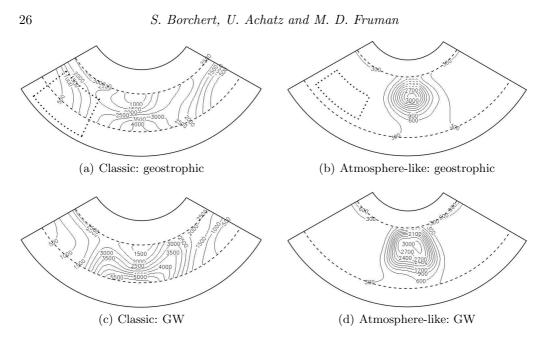(c) Classic: GW   (d) Atmosphere-like: GW

FIGURE 7. Contribution to the total energy by the various linear modes of the small-scale structures, defined as the differences between the simulated flow (of which the pressure and the horizontal divergence are shown in figure 6) and a smoothed flow obtained by a moving average. Shown is the energy contained in the geostrophic mode (a and b), and the energy of the two gravity wave modes (c and d), in arbitrary units, for the classic configuration (left column), and for the atmosphere-like configuration (right column). The dashed lines define the sub-region analysed and the dotted lines indicate the approximate horizontal size of the box used for the moving average and subsequent linear analysis.